Journal of Zhejiang University-SCIENCE A (Applied Physics & Engineering) in press
www.jzus.zju.edu.cn; www.springer.com/journal/11582
E-mail: jzus_a@zju.edu.cn

Research Article

https://doi.org/10.1631/jzus.A2400544

Study of the effect of flow frames on the performance of a 10 kW 40 kWh vanadium redox flow battery using a multi-scale model

Junhong LIN[1], Zihao MA[2], Shaojun LIU[1]✉, Hao SONG[1]✉, Guoneng LI[3], Weihong WU[1], Chenghang ZHENG[1], Xiang GAO[1]✉

[1]*State Key Laboratory of Clean Energy Utilization, State Environmental Protection Center for Coal-Fired Air Pollution Control, Zhejiang University, Hangzhou 310027, China*
[2]*Shanghai Electric Group Co. Ltd., Shanghai 200336, China*
[3]*Department of Energy and Environment System Engineering, Zhejiang University of Science and Technology, Hangzhou, 310023, China*

Abstract: The cell structure in vanadium redox flow batteries (VRFBs) critically impacts battery efficiency. Therefore, in this study we evaluate the effect of different flow frames on VFRB cell performance and system efficiency. This is accomplished through a multi-scale model combining a 3D model of the cell and an equivalent circuit model (ECM) of the stack. The results reveal that during the discharge process, increasing the flow rate can boost the discharge voltage, but also leads to higher pumping power consumption. Moreover, the pressure drop of the cell decreases as the number of flow frame channels increases. Due to improved reactant concentration distribution, the five-channel flow frame has a higher discharge voltage than other configurations at low reactant concentrations, even exceeding that of the twenty-channel flow frame. The flow frame structure and flow rate were optimized for a 10kW/40kWh VRFB with a genetic algorithm approach. Using a five-channel flow frame, a peak discharge efficiency of 93.70% was obtained at a flow rate of 960 mL/min. The results of this study may aid future design of kilowatt-scale VRFBs.

Key words: Flow frames; All vanadium redox flow battery; Multi-scale model; Genetic algorithm; Battery efficiency

1 Introduction

With the rapid growth of clean energy sources such as solar and wind power, energy storage technologies such as lithium-ion (Guo et al., 2023; Park et al., 2023; Guo et al., 2025) and flow batteries (Zerrahn and Schill, 2017; Albertus et al., 2020; Lu et al., 2024) are receiving increasing attention. In addition to benefits of long-duration energy storage and recyclability, flow batteries are intrinsically safer than lithium-ion batteries, due to the non-flammable aqueous electrolyte used. The flow field design critically affects the performance of flow batteries. For vanadium flow batteries, elaborate electrolyte channels are typically carved in the electrodes (Yang et al., 2022; Bhattarai et al., 2019) or bipolar plates (Zeng et al., 2019; Zheng et al., 2016); specially designed flow frames are also used to regulate the flow field. The configuration of such channels has been extensively investigated. For instance, Ali et al. (2022) compared the performance of serpentine and interdigitated channels, showing that 2 mm serpentine flow channels resulted in higher cell voltage and more uniform V^{2+} concentration in the negative electrode. However, serpentine flow channels also resulted in higher pump power consumption. Thus, Lu et al. (2021) optimized the discharge power and system efficiency of serpentine flow channels, demonstrating power and system efficiency that reached 16.73 W and 87.8%, respectively; these values were 2.85 W and 3.7% higher than the conventional approach. Sharma and Kumar (2021) also improved serpentine channels with two new designs: split serpentine and split-merged serpentine channels. Their experiments demonstrated better electrolyte distribution in the

---

✉ Shaojun LIU, phoenix205@zju.edu.cn
Shaojun LIU, https://orcid.org/0000-0003-0976-5707

Received Nov. 23, 2024; Revision accepted Apr. 7, 2025;
Crosschecked

split serpentine channel. Additionally, Gundlapalli and Jayanti (2021) proposed a flip-flop directional split serpentine flow field, which demonstrated excellent distribution and quick evacuation of product species. Their novel channel configuration ensures scaling from 900 to 2200 cm^2 of active cell area.

Designing cells with large active area is becoming more common in industrial practice, but has not been extensively studied (Ponce de León et al., 2006; Sun et al., 2019). A large active area can effectively reduce the number of cells in the stack, which is more conducive to VRFB applications (Sun et al., 2019). Several cells can be connected to form a stack, enabling kW-scale VRFB systems. In such systems, channels carved in the flow frames (instead of bipolar plates) are extensively employed to reduce material costs (Kim et al., 2013; Delgado et al., 2022; Guarnieri et al., 2018). However, this usually leads to kW-scale VRFBs having lower energy efficiency compared to batteries employing laboratory-scale equipment (Kapoor and Verma, 2022).

Only a few studies have investigated the effect of flow frames and achieved kW-scale VRFBs. For example, Kim et al. (2013) demonstrated a flow frame design in a 1kW/1kWh VRFB, with the average energy efficiency reaching 82% at a low current density of 80 mA/cm². And Guarnieri et al. (2018) tested a 9kW/26kWh VRFB with 40 cells, in which the flow frames followed an equal path length design.

In a typical cell, good electrochemical performance is always accompanied by an increased pressure drop. However, the conventional equivalent circuit model (ECM) for VRFBs (Delgado et al., 2022; Zhao et al., 2023) is unable to calculate this pressure drop. It also cannot represent the dynamics of cell voltage during battery operation. For this reason, we propose a multi-scale model which combines a 3D model of the cell with an ECM of the stack. Using this model, the effect of different flow frames on the performance of a 10 kW/40kWh vanadium redox flow battery are investigated. Varying structures are compared in terms of VRFB system efficiency and cell performance.

2 Numerical modeling

2.1 VRFB description

As shown in Fig. 1, the studied VRFB consists of an electrical stack, two electrolyte storage tanks, two pumps, and connecting pipes. The stack is comprised of multiple cells connected in series. A cell consists of two porous electrodes and an ion exchange membrane between them. Two tanks are used to store the anolyte and catholyte. During operation, electrolyte is pumped into the porous electrode and electrochemical reactions take place. The reactions at the electrodes are described by Eqs. (1) and (2).

Positive electrode:

$$\mathrm{VO^{2+} + H_2O - e^- \rightleftharpoons VO_2^+ + 2H^+} \qquad (1)$$

Negative electrode:

$$\mathrm{V^{3+} + e^- \rightleftharpoons V^{2+}} \qquad (2)$$

The state of charge (SOC) is used to describe the relative amount of vanadium ions with different valences, in both the porous electrodes and the tanks. It is defined as follows:

$$\mathrm{SOC} = \frac{c(\mathrm{V^{2+}})}{c(\mathrm{V_{total}})} = \frac{c(\mathrm{V^{5+}})}{c(\mathrm{V_{total}})} \qquad (3)$$

where $c(\mathrm{V^{2+}})$ and $c(\mathrm{V^{5+}})$ are the molar concentrations of $\mathrm{V^{2+}}$ and $\mathrm{VO_2^+}$, respectively, and $c(\mathrm{V_{total}})$ is the total vanadium ion concentration in a given electrolyte.

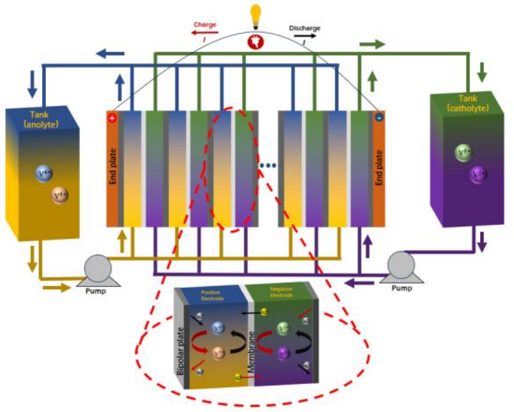

Fig. 1 Schematic diagram of the vanadium redox flow battery

2.2 Description of the VRFB cell

In this work, a three-dimensional (3D) VRFB cell was constructed. The VRFB cell consists of porous electrodes, current collectors, a proton exchange membrane, bipolar plates, and flow frames, as shown in Fig. 2. Flow channels were carved into the flow frame to provide a steady electrolyte supply. Three flow frames with different numbers of channels were compared in terms of flow field and electrochemical performance. The 3D model enables detailed analysis of cell performance and can act as a reference for design optimization. In the assembly and sealing of the cells, the channel depth in the flow frames will be lower than the thickness of the electrodes. The width of the channels and the position of the inlet were kept consistent for the three flow frames. The geometric parameters of the VRFB cell are listed in Table 1.

Table 1 Geometric parameters of the VRFB cell

Parameters	Value	Unit
Cell height	300	mm
Cell width	600	mm
Channel depth	1.3	mm
Electrode thickness	3.5	mm
Membrane thickness	50	μm

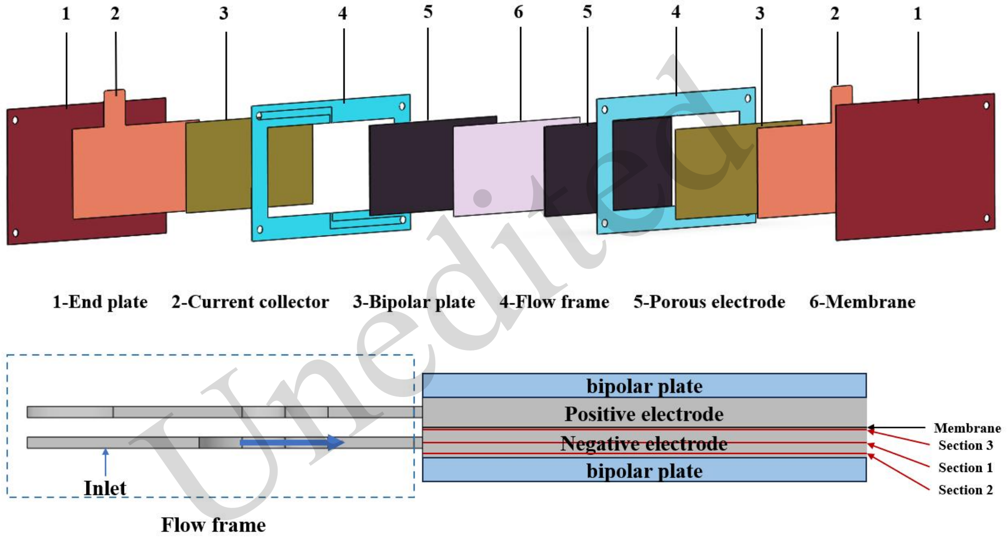

Fig. 2 Schematic diagram of the components used in a VRFB cell

2.3 Governing equations

2.3.1 Fluid flow in the frames and electrodes

The flow of electrolyte is described by the Navier-Stokes equation:

$$\rho(\boldsymbol{u}\cdot\nabla)\boldsymbol{u} =- \nabla p + \mu\nabla^2\boldsymbol{u} \tag{4}$$

$$\nabla\cdot\boldsymbol{u} = 0 \tag{5}$$

where $\boldsymbol{u}$ is the velocity of the electrolyte, ρ is the electrolyte density, μ is the dynamic viscosity of the electrolyte, and p is the pressure of the liquid.

The flow of electrolyte in a porous electrode is described by Darcy's law:

$$\boldsymbol{u} =- \frac{K}{\mu}\nabla p \tag{6}$$

where K is the permeability of the porous electrode. This permeability can be described by the Kozeny-Carman equation as follows:

$$K = \frac{\mathrm{d}_{\mathrm{f}}^2\varepsilon^3}{K_{\mathrm{ck}}(1-\varepsilon)^2} \tag{7}$$

where K_{ck} is the Kozeny-Carman constant, d_{f} is the fiber diameter, and ε is the electrode porosity.

2.3.2 Ions in the electrodes

The ions in the positive and negative electrodes are mainly comprised of vanadium ions (V^{2+}, V^{3+}, VO^{2+}, VO_2^+) and ion products from sulfuric acid (H^+, HSO_4^-, SO_4^{2-}). Each ion obeys the following conservation equation:

$$\frac{\partial}{\partial t}(\varepsilon c_j) + \nabla\cdot\left(- D_j^{\mathrm{eff}}\nabla c_j - z_j\kappa_j F c_j\nabla\varphi_j + \boldsymbol{u}c_j\right) =- S_j \tag{8}$$

where j represents a particular ion, c_j is the concentration of the ion, and D_j^{eff} denotes the effective diffusion coefficient of the ion in the porous electrode; z_j and κ_j indicate the valence of the ion and the ionic mobility, respectively; F is the Faraday constant; φ_j denotes the ionic potential in the electrodes, and S_j indicates the source term of the ion.

Electrolyte solutions are electrically neutral, therefore:

$$\sum_j z_j c_j = 0 \tag{9}$$

The diffusion of ions in VRFBs occurs in porous electrodes, which differs from behavior in free space. The ideal ion diffusion coefficients are corrected with the Bruggeman equation:

$$D_j^{\mathrm{eff}} = \varepsilon^{1.5} D_j \tag{10}$$

where D_j denotes the diffusion coefficient of the ion in free space.

The source term describes how ion concentrations change in the electrolyte due to electrochemical reactions or the dissociation of sulfuric acid, as shown in Table 2 (here, $\boldsymbol{i}$ denotes the current density).

Table 2 The source terms of the conservation equation

Source term	Positive electrode	Negative electrode
$S_{\mathrm{V}^{2+}}$	-	$\nabla\cdot\boldsymbol{i}/F$
$S_{\mathrm{V}^{3+}}$	-	$-\nabla\cdot\boldsymbol{i}/F$
$S_{\mathrm{V}^{4+}}$	$\nabla\cdot\boldsymbol{i}/F$	-
$S_{\mathrm{V}^{5+}}$	$-\nabla\cdot\boldsymbol{i}/F$	-
S_{H^+}	$-S_{\mathrm{HSO}_4^-}$	$-2\nabla\cdot\boldsymbol{i}/F - S_{\mathrm{HSO}_4^-}$
$S_{\mathrm{HSO}_4^-}$	$S_{\mathrm{HSO}_4^-}$	$S_{\mathrm{HSO}_4^-}$

2.3.3 Transport in the membrane

In a proton exchange membrane, it is assumed that protons are the only mobile ions. The current conservation equation can be expressed as follows:

$$\boldsymbol{N}_{\mathrm{H}^+} = -\frac{\sigma_{\mathrm{mem}}}{F}\nabla\phi_{\mathrm{mem}} \tag{11}$$

where σ_{mem} is the membrane conductivity, ϕ_{mem} is the membrane potential, and $\mathrm{N}_{\mathrm{H}^+}$ is the flux density vector of protons.

2.3.4 Electrochemical kinetics

The Butler-Volmer model was used to describe the relationship between current density and overpotential during the electrochemical reactions:

$$J_1 = A_{\mathrm{S}} F k_1 (c_{\mathrm{V}^{4+}})^{(1-\alpha_1)} (c_{\mathrm{V}^{5+}})^{\alpha_1} \left[\frac{c_{V^{4+}}^{s}}{c_{V^{4+}}}\exp\left(\frac{(1-\alpha_1)F\eta_1}{R_{\mathrm{g}}T}\right) - \frac{c_{\mathrm{V}^{5+}}^{\mathrm{s}}}{c_{\mathrm{V}^{5+}}}\exp\left(-\frac{\alpha_1 F\eta_1}{R_{\mathrm{g}}T}\right)\right] \tag{12}$$

$$J_2 = A_{\mathrm{S}} F k_2 (c_{\mathrm{V}^{2+}})^{(1-\alpha_2)} (c_{\mathrm{V}^{3+}})^{\alpha_2} \left[\frac{c_{V^{2+}}^{s}}{c_{V^{2+}}}\exp\left(\frac{(1-\alpha_2)F\eta_2}{R_{\mathrm{g}}T}\right) - \frac{c_{\mathrm{V}^{3+}}^{\mathrm{s}}}{c_{\mathrm{V}^{3+}}}\exp\left(-\frac{\alpha_2 F\eta_2}{R_{\mathrm{g}}T}\right)\right] \tag{13}$$

Here, J_1 and J_2 are the transfer current densities of the positive and negative electrodes respectively; A_{s} is the specific surface area of the electrode; k_1 and k_2 are the reaction rate constants; α_1 and α_2 are the charge transfer coefficients; s represents the liquid–solid interfaces of the porous region; R_{g} is the universal gas constant; T is the temperature; η_1 and η_2 represent the activation overpotentials of the positive and negative reactions, respectively. η_1 and η_2 are defined as:

$$\eta_1 = \phi_{\mathrm{s}} - \phi_{\mathrm{l}} - E_1 \tag{14}$$

$$\eta_2 = \phi_{\mathrm{s}} - \phi_{\mathrm{l}} - E_2 \tag{15}$$

where ϕ_{s} is the electrode potential, ϕ_{l} is the electrolyte potential, and E_1 and E_2 are the standard equilibrium potentials for positive and negative redox reactions, respectively.

E_1 and E_2 are expressed by the Nernst equation:

$$E_1 = E_1^0 + \frac{R_{\mathrm{g}}T}{F}\ln\left(\frac{c_{\mathrm{V}^{5+}}(c_{\mathrm{H}^+})^2}{c_{\mathrm{V}^{4+}}}\right) \tag{16}$$

$$E_2 = E_2^0 + \frac{R_{\mathrm{g}}T}{F}\ln\left(\frac{c_{\mathrm{V}^{3+}}}{c_{\mathrm{V}^{2+}}}\right) \tag{17}$$

where E_1^0 and E_2^0 are the positive and negative standard potentials, respectively.

The cell voltage is calculated as follows:

$$E_{\mathrm{cell}} = E_1^0 - E_2^0 + \frac{R_{\mathrm{g}}T}{F}\ln\left(\frac{c_{\mathrm{V}^{2+}}c_{\mathrm{V}^{5+}}(c_{\mathrm{H}^+})^2}{c_{\mathrm{V}^{3+}}c_{\mathrm{V}^{4+}}}\right) - \eta_1 - \eta_2 - IR_{\mathrm{cell}} \tag{18}$$

Here, I denotes the discharge current of the cell, and R_{cell} is the cell's resistance.

2.4 Model parameters

Table 3 and Table 4 list the relevant parameters used in the 3D model of the VRFB cell.

Table 3 Model parameters of the VRFB cell

Parameters	Symbols	Value	Unit	Reference
Total vanadium ion concentration	$c(\mathrm{V}_{\mathrm{total}})$	1700	$\mathrm{mol/m^3}$	-

Initial proton concentration	$c^0(\mathrm{H}^+)$	4000	$\mathrm{mol/m^3}$	-
$\mathrm{HSO_4^-}$ ion concentration	$c^0(\mathrm{HSO_4^-})$	4000	$\mathrm{mol/m^3}$	-
$\mathrm{V^{2+}}$ diffusion coefficient	$D_{\mathrm{V^{2+}}}$	2.4×10^{-10}	$\mathrm{m^2/s}$	(Lee et al., 2019)
$\mathrm{V^{3+}}$ diffusion coefficient	$D_{\mathrm{V^{3+}}}$	2.4×10^{-10}	$\mathrm{m^2/s}$	(Lee et al., 2019)
$\mathrm{V^{4+}}$ diffusion coefficient	$D_{\mathrm{V^{4+}}}$	3.9×10^{-10}	$\mathrm{m^2/s}$	(Lee et al., 2019)
$\mathrm{V^{5+}}$ diffusion coefficient	$D_{\mathrm{V^{5+}}}$	3.9×10^{-10}	$\mathrm{m^2/s}$	(Lee et al., 2019)
$\mathrm{H^+}$ diffusion coefficient	$D_{\mathrm{H^+}}$	9.312×10^{-9}	$\mathrm{m^2/s}$	(Lee et al., 2019)
$\mathrm{SO_4^{2-}}$ diffusion coefficient	$D_{\mathrm{SO_4^{2-}}}$	1.065×10^{-9}	$\mathrm{m^2/s}$	(Lee et al., 2019)
$\mathrm{HSO_4^-}$ diffusion coefficient	$D_{\mathrm{HSO_4^-}}$	1.33×10^{-9}	$\mathrm{m^2/s}$	(Lee et al., 2019)
Universal gas constant	R_g	8.3145	$\mathrm{J/(mol\cdot K)}$	-
Faraday constant	F	96485	$\mathrm{C/mol}$	-
State of charge	SOC	0.8	-	-
Kozeny-Carman constant	K_ck	9	-	-
Density	ρ	1354	$\mathrm{kg/m^3}$	(Lee et al., 2019)
Viscosity	μ	4.928×10^{-3}	$\mathrm{Pa\cdot s}$	(Lee et al., 2019)
Specific surface area	A_s	1.62×10^{4}	$\mathrm{1/m}$	(Lee et al., 2019)
Carbon fiber diameter	d_f	1.76×10^{-5}	m	(Yuan et al., 2020)
Electrode conductivity	σ_ed	1000	S/m	(Lee et al., 2019)
Porosity	ε	0.90	-	-

Table 4 Parameters used in the simulation

Parameters	Symbols	Value	Unit	Reference
Positive rate constant	k_1	6.8×10^{-7}	m/s	(Lee et al., 2019)
Negative rate constant	k_2	1.7×10^{-7}	m/s	(Lee et al., 2019)
Positive transfer coefficient	α_1	0.55	-	(Lee et al., 2019)
Negative transfer coefficient	α_2	0.45	-	(Lee et al., 2019)
Positive standard potential	E_1^0	1.004	V	(Lee et al., 2019)
Negative standard potential	E_2^0	-0.255	V	(Lee et al., 2019)

2.5 Boundary conditions

The structure of the flow frame has a critical impact on the performance of the VFRB cells. In this study, the VRFB performance was tested for three different flow frame structures, as illustrated in Fig. 3. The walls of both the flow frames and the porous electrodes were assumed to satisfy no-slip boundary conditions. The positive and negative electrolyte flow rates were kept equal and ranged from 240-1080 mL/min. The mass flow inlet and outlet pressure boundary conditions were defined for the flow frames. The current density used in the discharge simulation was 105 mA/cm². The system temperature was held at 293.15 K. The equations governing the 3D numerical model of the cell were solved using COMSOL Multiphysics® software.

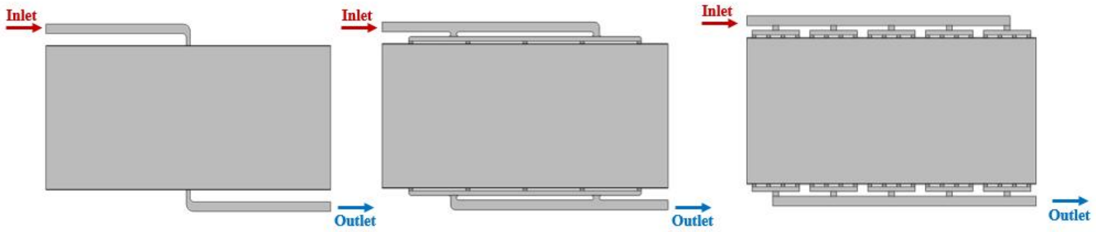

(a) Channel 1 (b) Channel 5 (c) Channel 20

Fig. 3 Flow frame designs for the numerical simulation

2.6 Mesh independence analysis

Effective mesh division can improve the

computational efficiency and accuracy of simulations. The 3D model of the VRFB was therefore investigated for mesh independence. The model was mainly divided into tetrahedral meshes, and the mesh was refined in corners and areas of complex flow, as shown in Fig. 4. To verify the independence between the simulation results and the number of meshes, four different mesh numbers were selected for comparative simulations. The mesh number increased proportionally from 1.15×10^6 to 1.22×10^7, with the obtained results shown in Fig. 5. Considering both the computational cost and accuracy, a mesh number over 6.20×10^6 was used for future comparison and discussion. We also compared structured and unstructured grids to validate the effectiveness of unstructured grids in this context. Fig. S1 shows the structured grid for Channel 1, and Fig. S2 compares the results of structured and unstructured grids. Both methods produce essentially the same results, showing that unstructured grids can flexibly and accurately treat complex geometries.

Fig. 4 Mesh refinement in the corners

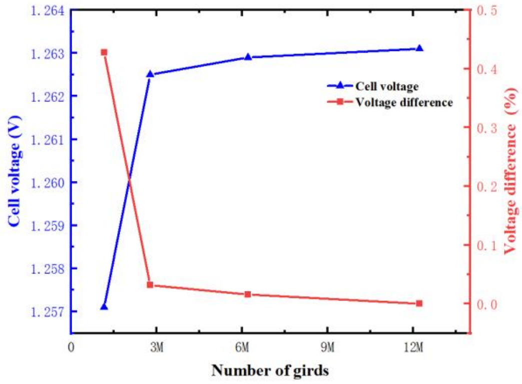

Fig. 5 Grid independence analysis

2.7 Multi-scale model of the VRFB

In the ECM of the VRFB, each cell is simplified to consist of a series-connected internal resistance and a controlled voltage source, where the internal resistance (R_{int}) is comprised of the component resistance and the contact resistance between components. The voltage of the controlled source is obtained by linear interpolation of the cell model simulation results under different operating conditions. The resistance of the porous electrodes and the proton exchange membrane are calculated in the cell model, so R_{int} represents only the resistance of the bipolar plate between the cells. The ECM uses the Simscape block in *MATLAB* to construct a circuit model with parallel and series ohmic resistors connected to controlled voltage sources (represented as cells of the VRFB), and a constant current source (used to simulate constant current discharge).

Shunt currents are generated by the flow of electrolytes in the stack manifolds, which form paths between individual cells connected in series. The paths can be simplified to equivalent resistances in the ECM. These resistances are calculated using Eq. (19):

$$R = \frac{l}{\sigma A} \tag{19}$$

where l is the effective length, A is the cross-sectional area, and σ is the electrolyte conductivity. R_{pc_j}, R_{nc_j}, R_{pm_j}, and R_{nm_j} denote the equivalent resistances of the electrolyte in the positive channel, the negative channel, the positive manifold, and the negative manifold, respectively, and j represents the j^{th} cell in the stack. The electrical conductivity σ depends on the SOC of the solution in each cell (Trovò et al., 2019):

$$\sigma_{\text{n}} = \text{SOC}\cdot\sigma_{\text{V}^{2+}} + (1-\text{SOC})\cdot\sigma_{\text{V}^{3+}} \tag{20}$$

$$\sigma_{\text{p}} = \text{SOC}\cdot\sigma_{\text{V}^{5+}} + (1-\text{SOC})\cdot\sigma_{\text{V}^{4+}} \tag{21}$$

where σ_{n} and σ_{p} is the catholyte and anolyte conductivity, respectively.

Additionally, species are exchanged between the stack and the tank during battery operation. The mass balance of the VRFB model is based on the following assumptions: (1) The electrolyte is completely mixed in the pipe, stack, and tank. (2) The charge loss during battery operation is caused only by the shunt current. The transport of species across the membrane is not considered. (3) Electrolyte parameters such as density, viscosity, and mobility remain constant during battery operation. (4) Flow rate differences between cells are not considered.

The ion concentration in the tanks is determined by the flow rate and the ion concentration at the stack outlet. The concentration in the tanks is calculated using the following equation (Han et al., 2024):

$$\frac{dc_i^{tank}}{dt} = \frac{Q}{V_{tank}}\left(c_i^{stack} - c_i^{tank}\right) \quad (22)$$

where c_i^{tank} is the concentration of the valence vanadium ion i in the tank, Q is the flow rate of the stack, V_{tank} is the volume of electrolyte in the positive/negative tank, and c_i^{tank} is the ion concentration at the outlet of the stack.

The concentration in the cell is controlled by both the flow rate and the electrochemical reaction. Moreover, it is assumed that the concentration distribution in the cell varies linearly, which is expressed as follows:

$$\frac{dc_i^{cellave_j}}{dt} = \frac{Q}{MV_{cell}}\left(c_i^{tank} - c_i^{cellout_j}\right) \pm \frac{I_j}{zFV_{cell}} \quad (23)$$

$$c_i^{cellave_j} = \left(c_i^{cellin_j} + c_i^{cellout_j}\right)/2 \quad (24)$$

$$c_i^{stack} = \sum_{j=1}^{M} c_i^{cell_j}/M \quad (25)$$

where $c_i^{cellin_j}$, $c_i^{cellout_j}$, and $c_i^{cellave_j}$ represent the average concentrations of the i-valent ions at the inlet, outlet, and the entire cell within the j^{th} cell, respectively, M is the number of cells, z is the unit activity coefficient, F is Faraday's constant, V_{cell} is the volume of electrolyte in the cell, and I_j is the charge/discharge current that flows through the j^{th} cell ($I > 0$ for charging). The sign of the value is determined by the species. When i equals 2 or 5, the value is positive; when i equals 3 or 4, the value is negative.

Therefore, the multi-scale model of the VRFB can be represented as shown in Fig. 6. I_L is the total discharge current of the stack. The parameters used in the multi-scale model are shown in Table 5. The currents and voltages in the circuit are calculated using Kirchhoff's law.

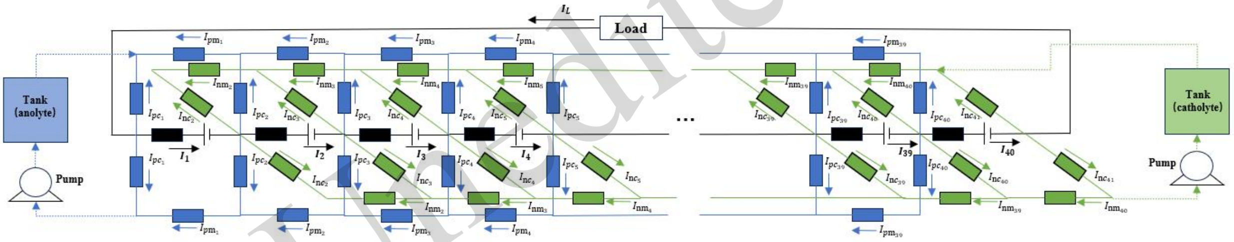

Fig. 6 The multi-scale model of a VRFB with 40 cells

Table 5 Parameters used in the multi-scale model of the VRFB

Parameters	Value	Unit	Reference	Meaning
R_{int}	1.6×10^{-7}	Ω	-	Bipolar plate resistance between cells
$\sigma_{V^{2+}}$	27.5	S/m	(Moro et al., 2017)	V^{2+} solution conductivity
$\sigma_{V^{3+}}$	17.5	S/m	(Moro et al., 2017)	V^{3+} solution conductivity
$\sigma_{V^{4+}}$	27.7	S/m	(Moro et al., 2017)	V^{4+} solution conductivity
$\sigma_{V^{5+}}$	41.3	S/m	(Moro et al., 2017)	V^{5+} solution conductivity
V_{tank}	0.75	m^3	-	Electrolyte volume in the tank
V_{cell}	0.00063	m^3	-	Electrolyte volume in the cell
l_m	0.008	m	-	Manifold length
A_m	4.91×10^{-4}	m^2	-	Manifold area
I_L	189	A	-	Stack discharge current
ψ_{pump}	0.9	-	(Ali et al., 2020)	Pump efficiency

3 Results and discussion

A major goal of this study is to analyze how the flow frame structure affects the VRFB performance. A properly distributed flow field in the porous electrodes of a VRFB cell can improve the battery performance. Hence, battery performance across different flow field distributions was investigated in terms of discharge voltage, pressure drop, and vanadium concentration. Finally, the effect of flow frame structure on system efficiency was analyzed using the multi-scale model of the VRFB. Given that mass transfer and electrochemical reactions in the positive and negative electrodes are essentially similar, only the negative electrode was used for comparative analysis.

3.1 Model validation

To validate the accuracy of the cell model, the discharge data from a single cell with an electrode size of 600 mm × 300 mm was tested. The initial and final vanadium ion concentrations were quantified by potentiometric titration to determine the corresponding state of charge (SOC). Constant current density discharge tests were conducted on the single cell experimental platform (shown in Fig. 7). During the experiment, the electrolyte flow rate was set to 1080 mL/min, and the applied current density was 105 mA/cm², which is consistent with the conditions in the numerical simulation. The VRFB discharge cutoff voltage was 1.1 V.

Fig. 8 compares the simulation and experimental results for the discharge voltage at different states of charge. The results indicate that the numerical model accurately reflects the behavior of the battery during discharge. In the low state of charge region, the discrepancy between the numerical results and the experimental results is more obvious. This is because the cell discharge voltage decreased rapidly at the end of discharge, which increased the error in estimating the reactant concentration during the discharge process.

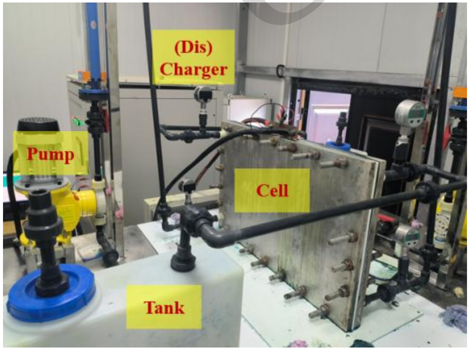

Fig. 7 Test platform for a cell of the VRFB

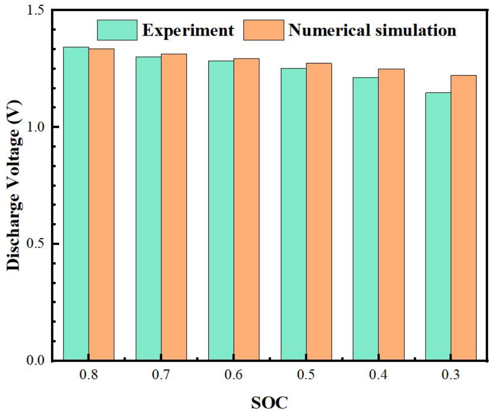

Fig. 8 Comparison of the numerical and experimental results

3.2 Velocity and pressure drop

The velocity distributions within the electrodes are significantly influenced by the configuration of the flow frames, as illustrated in Fig. 9. A large area of high values is clearly observed for Channel 1, which is located in the middle of the electrode. In contrast, high value areas for Channels 5 and 20 are only located near the top and bottom of the electrodes.

Fig. 10 depicts the effect of flow rate on velocity distribution. Over Section 1, velocities along a red line which is offset 30 mm from the top of the electrode (Line 1) were chosen for comparison. As expected, velocity differences increase with increasing flow rates for all flow frames. Interestingly, the number of velocity peaks is the same as the number of channels for Channels 1 and 5, coinciding with the velocity contour shown in Fig. 9. As channel numbers continue to increase, velocity peaks transform into velocity plateaus at Channel 20. A similar phenomenon can be observed along other lines, as evidenced by the velocity changes along lines 150 mm (Line 2) and 270 mm (Line 3) offset from the top of the electrode. Meanwhile, the velocity fluctuates relatively gently along Line 2. This is mainly due to the significant resistance exerted on the fluid by the porous electrode. According to Darcy's law, the higher the fluid velocity, the greater the resistance it encounters. This causes the fluid in regions with higher velocity to diffuse towards adjacent regions, leading to a more uniform velocity distribution. Additionally, we assessed velocity fluctuations by dividing the standard deviation of the velocity by its mean value. Along Line 1 and Line 3, Channels 5 and 20 show similar values. But along Line 2, Channel 5 has a more uniform velocity than Channel 20, implying a more even distribution of concentration.

Another key performance parameter for the cell is the pressure drop, which affects the amount of pump consumption during battery operation. An excessive pressure drop will reduce the system efficiency during the charge/discharge cycle, and also necessitate stronger mechanical properties for the components, which may increase manufacturing costs. Fig. 11 presents a comparison of the total pressure drops of different flow frames, at flow rates ranging from 240-1080 mL/min. An approximate positive linear relationship between total pressure drop and flow rate can be observed. The total pressure drop for Channel 1 reaches 5.3×10^4 Pa at a flow rate of 1080 mL/min, while the pressure drops for Channels 5 and 20 are relatively low. This may be because Darcy's law governs fluid flow in porous electrodes. The pressure drop in the electrodes is further illustrated in Fig. S3. A high value for Channel 1 is obvious, and Channel 5 and Channel 20 have almost the same values. Note that the total pressure drop of Channel 5 is higher than that of Channel 20, implying that the differences in the flow frames are responsible for this effect. Indeed, Channel 20 has a shorter electrolyte path in its flow frame compared to Channel 5, as shown in Fig. S4.

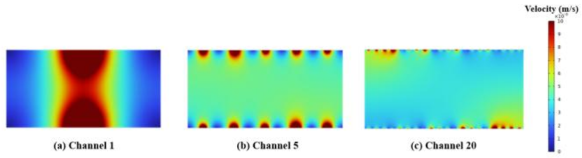

Fig. 9 The distribution of velocity (Section 1) at the negative electrode for all three flow frames (Q = 600 mL/min). (a) Channel 1, (b) Channel 5, (c) Channel 20

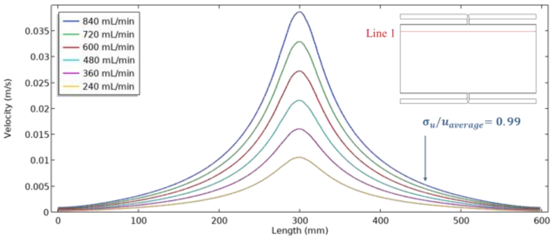

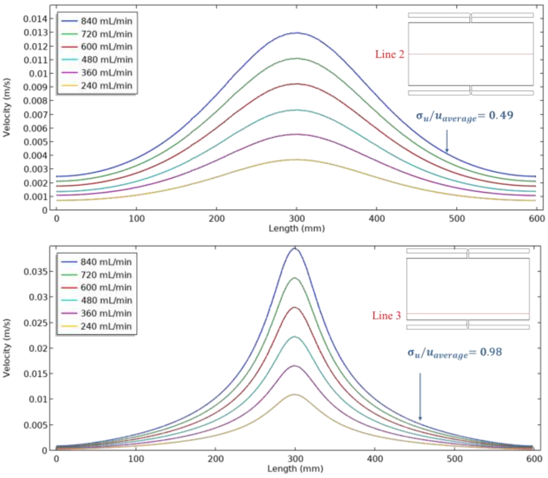

(a) Channel 1

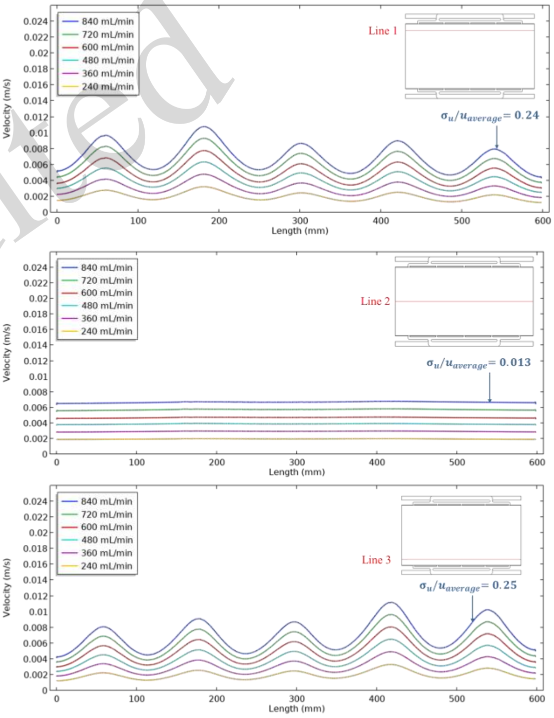

(b) Channel 5

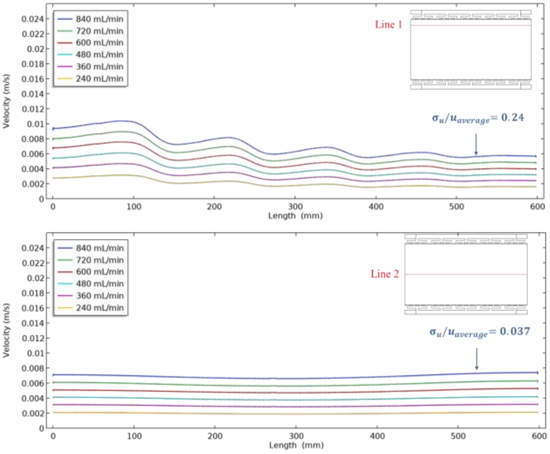

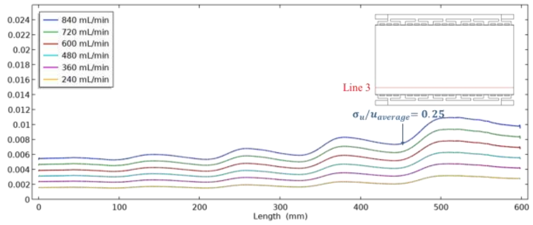

(c) Channel 20

Fig. 10 Velocity change along the red line for different flow frames (Section 1): (a) Channel 1, (b) Channel 5, (c) Channel 20

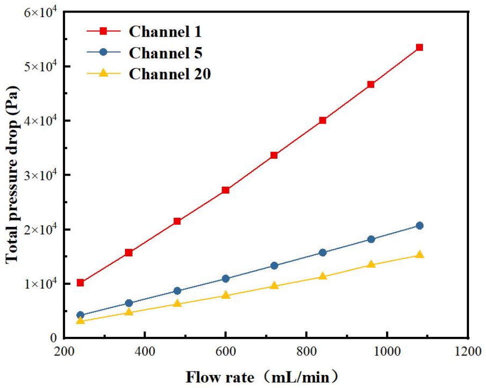

Fig. 11 Total pressure drop for different flow frames across various electrolyte flow rates

3.3 Discharge voltage and V^{2+} concentration distribution

Discharge voltage is an important factor in evaluating battery performance. Therefore, we compare the discharge voltage for the three flow frame structures across different flow rates. In the numerical simulations, the SOC is kept between 0.2-0.8 and the discharge current density is set at 105 mA/cm². The cut-off voltage was set to 1.1 V. The flow rates of catholyte and anolyte were equivalent, and were increased from 240 mL/min to 1080 mL/min. The discharge voltage of batteries with different flow frames across varying flow rates and SOCs is shown in Fig. 12. With an increasing flow rate, the discharge voltages of all three flow frames rise. This is because the higher flow rate can increase the concentrations of reactants in the electrodes. However when the reactant concentrations become sufficient, this effect becomes weaker; also, the voltage difference between the three flow frames decreases. Thus, the electrolyte flow rate is the main factor influencing the discharge process of the VRFB. The Channel 5 structure has a higher discharge voltage than the other structures, especially at low flow rates and SOCs. Interestingly, this contrasts with the speculation that more channels would lead to a more even distribution of velocity and a higher discharge voltage.

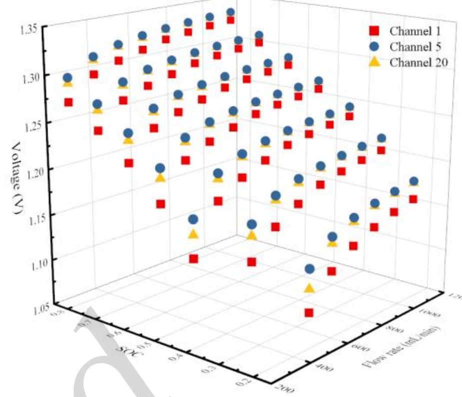

Fig. 12 3D scatter plot of discharge voltage for the three flow frames at varying flow rates and SOCs

We aim to explain this phenomenon by investigating the reactant concentration distribution in the negative electrode. In Fig. 13, the concentration distributions of V^{2+} in Sections 1, 2, and 3 are shown when the flow rate is 360 mL/min and the SOC is 0.3. Compared to Channel 5 and Channel 20, Channel 1 shows a large low-concentration region of V^{2+}, which would significantly hinder battery performance. For Channels 5 and 20, the V^{2+} concentration distributions are similar, with obvious high values near the diagonal lines. This phenomenon can be explained by the direction of the pressure gradient in the porous electrode. As depicted in Fig. S5, the pressure is high near the inlet and low near the outlet; this pressure gradient causes the fluid to flow from the inlet towards outlet. Accordingly, V^{2+} ions are transported along with the fluid, and follow the trend of the diagonal line.

To evaluate the reactant concentrations, total values were calculated and are shown in Fig. 13. The values over different sections follow the same order, that is, Channel 5 > Channel 20 > Channel 1. Moreover, this trend persists with increasing flow rates, as shown in Fig. S6. The superior value for Channel 5 may be a consequence of the more uniform velocity distribution. As mentioned above, along different lines for Channel 5, the velocity fluctuation values ($\sigma_u/u_{\text{average}}$) are 0.24, 0.013, and 0.25, which are always lower than their counterparts in Channel 20. Thus, the unique design of Channel 5 promotes a higher reactant concentration within the electrode, leading to lower concentration polarization and higher discharge voltage.

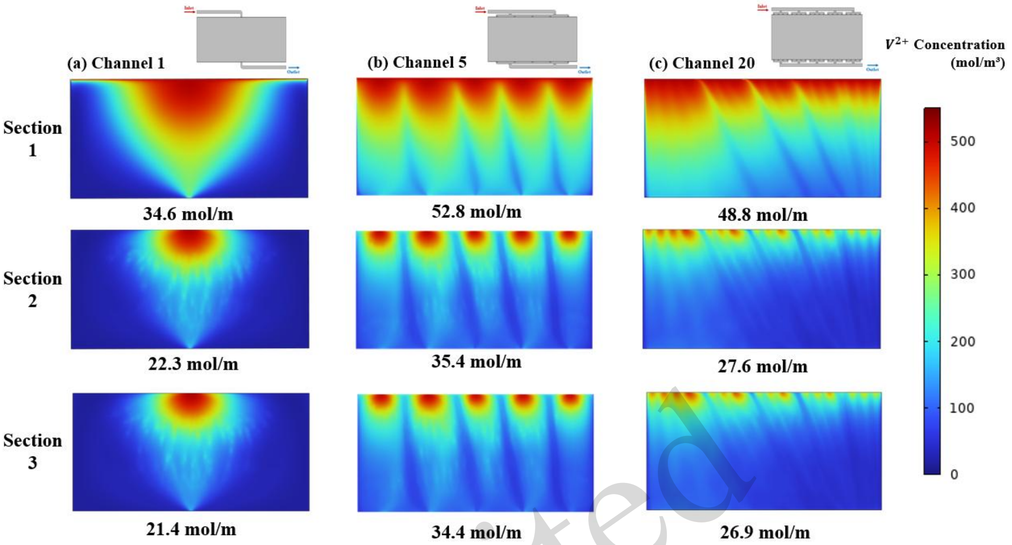

Fig. 13 V^{2+} concentration distribution and total values at different sections: (a) Channel 1, (b) Channel 5, and (c) Channel 20

3.4 Flow frame impact on system efficiency

Efficiency is a crucial parameter for evaluating the performance of a battery system. In the operation of a VRFB, increasing the electrolyte flow rate can enhance the stack voltage, but also leads to higher pump power consumption. Therefore, the selected flow rate needs to balance the electrochemical reaction and the pump power consumption. We use the system efficiency to comprehensively assess the impact of flow rate on these two aspects. To ascertain the optimal power efficiency using different cell structures, a 10kW/40kWh VRFB model with 40 cells was built. Then, the pump power of the entire stack and the power loss due to overpotential were investigated. The VRFB system efficiency (ψ_{power}) was calculated as follows:

$$\psi_{\text{power}} = \frac{P_{\text{net}}}{P_{\text{total}}} = 1 - \frac{P_{\text{loss}} + P_{\text{pump}}}{P_{\text{total}}} \tag{26}$$

$$P_{\text{loss}} = \sum_{j=1}^{M} I_j A \left(\eta_{\text{p}_j} + \eta_{\text{n}_j}\right) + P_{\text{R}} \tag{27}$$

$$P_{\text{pump}} = \frac{2(\Delta P_{\text{cell}} + \Delta P_{\text{G}}) \cdot Q}{\psi_{\text{pump}}} \tag{28}$$

where ψ_{power} is the VRFB system efficiency, ψ_{pump} is the pump efficiency, P_{net} is the output power, P_{total} is the total input power, P_{pump} is the pump power consumption, P_{loss} is the stack power loss, P_{R} is the stack ohmic power loss, ΔP_{cell} is the pressure drop in the cells, and ΔP_{G} is the gravitational potential difference between the tank and the stack that needs to be overcome.

The system efficiency of each flow frame at varying flow rates can be obtained from the VRFB model, as shown in Fig. 14. As the flow rate increases, the system efficiency of each flow frame gradually rises, and the gap between the efficiency of Channel 5 and Channel 20 gradually disappears. After the flow rate reaches 960 mL/min, increasing the flow rate has little effect on the system efficiency. A peak efficiency of 93.51% was observed at the electrolyte flow rate of 1080 mL/min for Channel 5 and Channel 20.

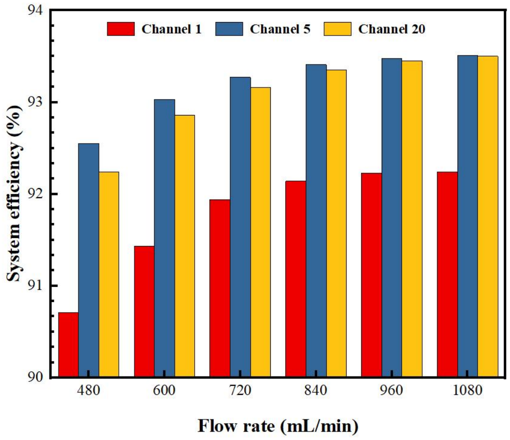

Fig. 14 System efficiency for various flow frame

structures at differing flow rates

From the ECM model, it was ascertained that an important parameter affecting the efficiency of the stack is the resistance of each cell. Among these resistances, R_{pm} and R_{nm} are determined by the thickness of the porous electrodes and bipolar plates; unfortunately, these are difficult to change. R_{pc} and R_{nc} can be increased by extending the lengths of the inlet/outlet pipes and shirking the pipe cross-section in the cell, so as to reduce the shunt current. However, this also increases the pressure drop as well as the pump consumption of the stack. Therefore we decide to use the genetic algorithm (GA) to optimize the parameters such as pipe length and cross-section width. Table 6 lists the optimization parameter ranges, and more detailed information on the GA workflow can be found in the Supporting Information. The upper limit of the flow rate is based on the pump's rated power, while the lower limit is set such that the system can operate normally without damaging the electrolyte. The maximum values for pipe length and cross-section width are constrained by the manufacturing precision. Our minimization objective (or objective function) is the VRFB’s system loss efficiency in the discharging process.

Table 6 Optimization parameters and ranges

Parameters	range	Unit
Pipe length of the positive side (L_{p})	0 - 3	m
Pipe length of the negative side (L_{n})	0 - 3	m
Pipe cross-section width of the positive side (W_{p})	10 - 60	mm
Pipe cross-section width of the negative side (W_{n})	10 - 60	mm
Flow rate (Q)	360-1080	mL/min

The optimal solutions obtained are shown in Table 7. Each solution includes the optimal sizes and the corresponding system efficiency of the discharge process. The highest efficiency of 93.70% was observed for Channel 5 at an electrolyte flow rate of 960 mL/min.

Table 7 Optimization results

Channel	L_{n} (m)	L_{p} (m)	W_{n} (mm)	W_{p} (mm)	Q (mL/min)	ψ_{power}
1	1.263	1.708	58	59	1080	92.65%
5	1.555	1.697	60	52	960	93.70%
20	1.141	1.709	45	53	977	93.63%

4 Conclusions

The performances of three different flow frame structures in a vanadium redox flow battery (VRFB) were evaluated at both the cell and stack level. To analyze the flow field and species concentration distribution at the cell level, a 3D model of the VFRB cells was developed. With this model, the cell performance was compared across different flow rates and states of charge (SOC), investigating factors such as pressure drop, velocity distribution, reactant concentration distribution, and discharge voltage. The results showed that the pressure drop of the cell decreases gradually with increasing numbers of channels in the flow frame. The cell with a five-channel flow frame was superior to the other configurations at low reactant concentration. We also found that despite a high flow rate enabling satisfactory discharge voltage, it also causes extra pumping consumption. Next, we proposed an equivalent circuit model (ECM) of the stack to simulate the operation of the battery. The system efficiency of the discharge process was used to evaluate different cell structures. The voltage differences between cells and the conductivity of the electrolyte generates shunt currents within the stack and piping system, which lead to energy losses and reduced system efficiency. The cell parameters affecting the shunt current in the discharge process were therefore optimized using a genetic algorithm. The final optimized configuration, using a five-channel flow frame, achieved a maximum system efficiency of 93.70% at a flow rate of 960 mL/min.

Acknowledgments

This work is supported by the ‘Pioneer’ and ‘Leading Goose’ R&D Program of Zhejiang Province (No.2024C03116), and the National Natural Science Foundation of China (42341208, 52206119).

Author contributions

Xiang Gao and Hao Song conceived the idea and designed the research. Junhong Lin, Zihao MA, Guoneng LI, Weihong Wu, and Chenghang Zheng performed the experiment. Junhong Lin, and Shaojun Liu analyzed the data and wrote the manuscript. All authors contributed to the discussion of the manuscript.

Conflict of interest

Junhong LIN, Zihao MA, Shaojun LIU, Hao SONG, Guoneng LI, Weihong WU, Chenghang ZHENG, and Xiang GAO declare that they have no conflict of interest.

References

Albertus P, Manser JS, Litzelman S, 2020. Long-Duration Electricity Storage Applications, Economics, and Technologies. *Joule*, 4(1): 21-32. https://doi.org/10.1016/j.joule.2019.11.009

Ali E, Kim J, Park H, 2022. Numerical analysis of modified channel widths of serpentine and interdigitated channels for the discharge performance of vanadium redox flow batteries. *Journal of Energy Storage*, 53: 105099. https://doi.org/10.1016/j.est.2022.105099.

Ali E, Kwon H, Kim J, et al., 2020. Numerical study on serpentine design flow channel configurations for vanadium redox flow batteries. *Journal of Energy Storage*, 32: 101802. https://doi.org/10.1016/j.est.2020.101802

Bhattarai A, Wai N, Schweiss R, et al., 2019. Vanadium redox flow battery with slotted porous electrodes and automatic rebalancing demonstrated on a 1 kW system level. *Applied Energy*, 236: 437-43. https://doi.org/10.1016/j.apenergy.2018.12.001

Delgado NM., Monteiro R, Cruz J, et al., 2022. Shunt currents in vanadium redox flow batteries – a parametric and optimization study. *Electrochimica Acta*, 403: 139667. https://doi.org/10.1016/j.electacta.2021.139667

Guarnieri M, Trovò A, D'Anzi A, et al., 2018. Developing vanadium redox flow technology on a 9-kW 26-kWh industrial scale test facility: Design review and early experiments. *Applied Energy*, 230: 1425-34. https://doi.org/10.1016/j.apenergy.2018.09.021

Gundlapalli R, Jayanti S, 2021. Effective splitting of serpentine flow field for applications in large-scale flow batteries. *Journal of Power Sources*, 487: 229409. https://doi.org/10.1016/j.jpowsour.2020.229409

Guo F, Wu X, Liu L, et al., 2023. Prediction of remaining useful life and state of health of lithium batteries based on time series feature and savitzky-golay filter combined with gated recurrent unit neural network. *Energy*, 270: 126880. https://doi.org/10.1016/j.energy.2023.126880

Guo S, Li X, Zhang Z, et al., 2025. Advancements in lithium solid polymer batteries: Surface modification, in-situ/operando characterization, and simulation methodologies. *Energy Materials*, 5: 500041. https://doi.org/10.20517/energymater.2024.214

Han A, Huang QS, Zhang QN, et al., 2024. Effect of Flow Rate Control Modes on a Vanadium Redox Flow Battery Based on a Numerical Model. *Korean Journal of Chemical Engineering*, 41: 1703-14. https://doi.org/10.1007/s11814-024-00152-y

Kapoor M, Verma A, 2022. Technical benchmarking and challenges of kilowatt scale vanadium redox flow battery. *WIREs Energy and Environment*, 11(5). https://doi.org/10.1002/wene.439

Kim S, Thomsen E, Xia GG, et al., 2013. 1 kW/1 kWh advanced vanadium redox flow battery utilizing mixed acid electrolytes. *Journal of Power Sources*, 237: 300-09. https://doi.org/10.1016/j.jpowsour.2013.02.045

Lee J, Kim J, Park H, 2019. Numerical simulation of the power-based efficiency in vanadium redox flow battery with different serpentine channel size. *International Journal of Hydrogen Energy*, 44(56): 29483-92. https://doi.org/10.1016/j.ijhydene.2019.05.013

Lu MY, Jiao YH, Tang XY, et al., 2021. Blocked serpentine flow field with enhanced species transport and improved flow distribution for vanadium redox flow battery. *Journal of Energy Storage*, 35: 102284. https://doi.org/10.1016/j.est.2021.102284

Lu Y, Shao Z, Lu H, 2024. Quantification of anthropogenic heat and simulation of its effects on environment and climate: A comprehensive review. *Renewable and Sustainable Energy Reviews*, 204: 114802. https://doi.org/10.1016/j.rser.2024.114802

Moro F, Trovò A, Bortolin S, et al., 2017. An alternative low-loss stack topology for vanadium redox flow battery: Comparative assessment. *Journal of Power Sources*, 340: 229-41. https://doi.org/10.1016/j.jpowsour.2016.11.042

Park S, Chaudhary R, A Han S, et al., 2023. Ionic conductivity and mechanical properties of the solid electrolyte interphase in lithium metal batteries. *Energy Materials*, 3: 300005. https://doi.org/10.20517/energymater.2022.65

Ponce LC, Frías-Ferrer A, González-García J, et al., 2006. Redox flow cells for energy conversion. *Journal of Power Sources*, 160(1): 716-32. https://doi.org/10.1016/j.jpowsour.2006.02.095

Sharma H, Kumar M, 2021. Enhancing power density of a vanadium redox flow battery using modified serpentine channels. *Journal of Power Sources*, 494: 229753. https://doi.org/10.1016/j.jpowsour.2021.229753

Sun J, Zheng ML, Yang ZS, et al., 2019. Flow field design pathways from lab-scale toward large-scale flow batteries. *Energy*, 173: 637-46. https://doi.org/10.1016/j.energy.2019.02.107

Trovò A, Marini G, Sutto A, et al., 2019. Standby thermal model of a vanadium redox flow battery stack with crossover and shunt-current effects. *Applied Energy*, 240: 893-906. https://doi.org/10.1016/j.apenergy.2019.02.067

Yang F, Qu DW, Chai YW, et al., 2022. Development of three-dimensional model for the analysis of the mass transport in vanadium redox flow batteries. *International Journal of Hydrogen Energy*, 47(64): 27358-73. https://doi.org/10.1016/j.ijhydene.2022.06.091

Yuan CG, Xing F, Zheng Q, et al., 2020. Factor analysis of the uniformity of the transfer current density in vanadium flow battery by an improved three-dimensional transient model. *Energy*, 194: 116839. https://doi.org/10.1016/j.energy.2019.116839

Zeng YK, Li FH, Lu F, et al., 2019. A hierarchical interdigitated flow field design for scale-up of high-performance redox flow batteries. *Applied Energy*, 238: 435-41. https://doi.org/10.1016/j.apenergy.2019.01.107

Zerrahn A, Schill WP, 2017. Long-run power storage requirements for high shares of renewables: review and a new model. *Renewable and Sustainable Energy Reviews*, 79: 1518-34. https://doi.org/10.1016/j.rser.2016.11.098

Zhao XB, Kim YB, Jung S, 2023. Shunt current analysis of vanadium redox flow battery system with multi-stack connections. *Journal of Energy Storage*, 73: 109233. https://doi.org/10.1016/j.est.2023.109233

Zheng Q, Xing F, Li XF, 2016. Flow field design and optimization based on the mass transport polarization regulation in a flow-through type vanadium flow battery. *Journal of Power Sources*, 324: 402-11. https://doi.org/10.1016/j.jpowsour.2016.05.110

中文概要

题　　目：基于多尺度模型研究电极框流道对 10kW 40kWh 钒液流电池性能的影响

作　　者：林俊宏[1]，马子豪[2]，刘少俊[1]，宋浩[1]，李国能[3]，吴卫红[1]，郑成航[1]，高翔[1]

机　　构：[1]浙江大学，能源清洁利用国家重点实验室，中国杭州，310027；[2]上海电气集团有限公司，中国上海，200336；[3]浙江科技大学，能源与环境系统工程系，杭州，310023

目　　的：钒液流电池的单电池结构对系统效率影响显著。本文旨在评估不同电极框流道对10kW/40kWh VFRB 电池性能及系统效率的影响，通过构建多尺度模型（结合单电池的三维模型与电堆等效电路模型）优化电池设计。

创新点：1. 揭示流场和离子浓度分布对单电池性能的影响；2. 提出多尺度模型，能够模拟 VRFB 充放电过程并评估系统性能；3. 基于遗传算法对 VRFB 进行优化。

方　　法：1. 验证了单电池模型有效性，并模拟不同流道下单电池内部流场分布（图 7-11）；2. 通过不同工况下的仿真结果，分析流道结构、流量和 SOC 等对离子浓度分布和放电电压影响规律（图 12、13）；3. 基于遗传算法得到 VRFB 参数优化方案（表 7）。

结　　论：1. 电极框流道的通道数量对电池的压降有显著影响，随着通道数量增加，单电池总压降逐渐减小；2. 五通道结构放电电压优于其他结构，在低流速和 SOC 下也能达到相对较高的放电电压。；3. 提高电解液流量虽能提升放电电压，但会导致泵耗增加。五通道结构经遗传算法优化后，在 960 mL/min 流量下，系统放电效率最高达到 93.70%。

关键词：电极框流道；全钒液流电池；多尺度模型；遗传算法；电池效率